Originally published as:

Key Points:
- Larger longitudinal differences at nighttime than daytime and greater in the south than the north
- Air pressure gradient caused by the day-night difference in solar heating is a major contributor
- Ion drag, viscous drag, and Coriolis forces play negative roles and show local time variations

Correspondence to:
H. Wang,
h.wang@whu.edu.cn

Longitudinal variation in zonal winds at subauroral regions: Possible mechanisms

Hui Wang[1] and Hermann Lühr[1,2]

[1]Department of Space Physics, School of Electronic Information, Wuhan University, Hubei, China, [2]GFZ German Research Center for Geosciences, Potsdam, Germany

Abstract Longitudinal differences in thermospheric zonal winds (ΔUy) are investigated in the subauroral region for different seasons and under solar maximum and medium conditions by using Challenging Minisatellite Payload observations. Prominent wave-1 longitudinal and diurnal variations of ΔUy are observed, along with an antiphase relationship between the Northern and Southern Hemispheres. These structures persist over the whole year and are independent of solar activity. ΔUy values are greater at nighttime than at daytime, and values in the south are greater than those in the north in local summer and winter. Model simulations confirm observed results in large-scale structures, and the nonzero dipole tilt is found to be vital for the longitudinal variation of the zonal wind. The neutral air pressure gradient caused by the day-night difference in solar heating is a major contributor to the observed ΔUy. The pressure effects are larger at nighttime than at daytime and larger in the Southern Hemisphere than in the Northern Hemisphere. Ion drag reduces the compatibility between the modeled and observed ΔUy as expected, with larger effects at nighttime than at daytime. Viscous force also reduces the compatibility between the modeled and observed ΔUy with greater effects at daytime, except at nighttime in the Southern Hemisphere. Similarly, the Coriolis force makes the difference between the modeled and observed ΔUy larger. The sum of these factors can explain, in general, the observed local time and hemispheric asymmetry features in longitudinal variation of the zonal wind.

1. Introduction

Thermospheric winds play an important role in the ionosphere-thermosphere coupling process. They can transport plasma along magnetic field lines [e.g., *Rishbeth*, 1967] and generate electric fields via the dynamo effect [e.g., *Blanc and Richmond*, 1980]. They are also a major cause of observed local time, seasonal changes, and interhemispheric and longitudinal differences of the ionospheric electron densities at low and middle latitudes (e.g., see review papers by *Rishbeth* [1972] and *Titheridge* [1995]). Therefore, it is essential to study the spatial distribution of thermospheric winds to better understand ion-neutral interactions and to improve space weather modeling and forecasting abilities.

During the past few decades, thermospheric winds have been studied extensively using nighttime observations from Fabry-Perot interferometers (FPIs) [*Rees et al.*, 1980; *Sipler et al.*, 1982; *Killeen et al.*, 1986; *Fejer et al.*, 2002; *Hernandez and Roble*, 1984; *Wu et al.*, 2014a, 2014b; *Deng et al.*, 2014], incoherent scatter radar [*Sipler et al.*, 1991; *Aruliah et al.*, 1996; *Witasse et al.*, 1998; *Buonsanto and Witasse*, 1999], the Dynamics Explorer 2 satellite [*Thayer et al.*, 1987; *Killeen and Roble*, 1988], the Upper Atmosphere Research Satellite [*Fejer et al.*, 2000; *Emmert et al.*, 2001], and the Challenging Minisatellite Payload (CHAMP) satellite [e.g., *Liu et al.*, 2006; *Lühr et al.*, 2007; *Doornbos et al.*, 2010; *Ritter et al.*, 2010; *Xiong et al.*, 2015a, 2015b], as well as numerical and empirical models [*Richmond*, 1992; *Hedin et al.*, 1996; *Ridley et al.*, 2006; *Codrescu et al.*, 2008; *Drob et al.*, 2008; *Emmert et al.*, 2008; *Sun et al.*, 2015].

Zonal winds at middle latitudes exhibit obvious diurnal (local time) and seasonal variations. During quiet times they are generally directed eastward from postnoon to early morning and westward otherwise. The crossover time from westward to eastward is in the postnoon sector at middle latitudes [*Liu et al.*, 2006; *Xiong et al.*, 2015a], while the crossover time from eastward to westward is seasonally dependent, with the earliest times being in June and the latest in December [*Fejer et al.*, 2002; *Deng et al.*, 2014]. *Hernandez and Roble* [1984] found that during solar minimum conditions, the nighttime-averaged zonal winds were predominantly eastward

during winter, at speeds of 50 – 75 m/s, and westward during the summer, at speeds of 50 – 100 m/s. Nighttime zonal winds at middle latitudes exhibit strong dependence on solar activity but only in winter when the ion drag effect is small [*Fejer et al.*, 2002].

Previous studies on disturbance zonal winds at middle latitudes during geomagnetically active periods found them to be dependent on local time. Winds were westward with large amplitudes in the premidnight sector, possibly related to subauroral polarization streams, and eastward with smaller amplitudes in the late night sector [*Fejer et al.*, 2002; *Emmert et al.*, 2006; *Erickson et al.*, 2011; *Wang et al.*, 2011; *Xiong et al.*, 2015a]. *Emmert et al.* [2001] found that the daytime zonal disturbance winds were mostly westward except in the early morning sector and had the largest amplitudes in the late afternoon sector. *Liu et al.* [2006] reported that at middle latitudes, the daytime zonal wind at CHAMP altitude were less sensitive to geomagnetic activities than nighttime winds. Others have observed that zonal wind perturbations increase roughly linearly with *Kp* and increasing latitudes [*Fejer et al.*, 2002; *Emmert et al.*, 2006; *Xiong et al.*, 2015a]. *Ritter et al.* [2010] were the first to report that the enhancement of the westward wind had an average amplitudes of about 50 m/s at middle latitude around midnight during substorm periods.

Interhemispheric comparisons of zonal winds at middle latitudes have been performed recently. *Deng et al.* [2014] found that the nighttime average zonal wind was predominantly westward at Palmer (54°S magnetic latitude, MLat, 64°W geographic longitude, GLon) and eastward at Millstone (53°N MLat, 71.5°W GLon). At equinox, the local time variation of neutral wind showed a very good conjugacy but at June solstice the similarity became less clear; this was attributed to the seasonal asymmetry of hemispheric polar activity. *Wu et al.* [2014a] compared the conjugacy of the zonal winds at Palmer and Millstone under three different geomagnetic activities and found that as compared to quiet time, more conjugacy was found during geomagnetically active periods when high-latitude effects became dominant.

With respect to longitudinal variations in zonal wind, previous work mainly focused on the equatorial regions [e.g., *Wu et al.*, 1994; *Lühr et al.*, 2007; *Häusler et al.*, 2007]. Relatively little attention has been paid to the middle (subauroral) latitudes: longitudinal averages have been used in previous studies. The underlying physical causes for the longitudinal differences in the zonal winds at subauroral latitudes are not clear. A few studies using ground FPI nighttime observations suggest that the geomagnetic latitude difference greatly affects the longitudinal differences in the thermospheric winds [*Hernandez et al.*, 1978; *Wu et al.*, 2014b]. *Hernandez et al.* [1978] used a pair of FPIs (Boulder: 40°N, 105°W, 49°N MLat and Laurel Ridge: 40°N, 79°W, 50°N MLat) with a 26° longitudinal separation between them to study longitudinal variations in solar minimum, magnetically quiet conditions. The thermospheric winds were found to be mostly consistent with each other because both stations were located at similar magnetic latitudes. *Wu et al.* [2014b] first reported longitudinal variations in zonal wind based on three FPIs located in the United States (Boulder) and China (Xinglong: 40°N, 115°E, 34°N MLat and Kelan: 39°N, 112°E, 33°N MLat) over two nights. The FPIs were separated by more than 100° in longitude. They found that the Boulder zonal winds exhibited larger diurnal variations than those in Xinglong and Kelan, because of its location at a higher geomagnetic latitude closer to the auroral oval. They proposed that the Joule heating effect, rather than the ion convection effect, would produce a larger pressure gradient near the auroral oval and would in turn caused larger diurnal variations in zonal winds at stations nearer to the auroral oval.

In this paper, we present the longitudinal and local time variations of the zonal winds observed by CHAMP in both the northern and southern subauroral regions (±50° to ±60° MLat) for four seasons and two solar activities. We used the global ionosphere and thermosphere model (GITM) to simulate thermospheric winds for comparison with our observations in order to understand the mechanisms for the longitudinal variations. We investigated various physical factors that might modulate the longitudinal distribution of the zonal winds, including magnetic field geometry, pressure gradient, ion drag, Coriolis force, viscous force, and solar extreme ultraviolet (EUV) flux. These factors are important for the development of zonal winds, but their role in longitudinal modulation have not been addressed in the literature from a global perspective.

2. CHAMP Data and GITM Model

The CHAMP mission lasted from 2000 to 2010. It had a near-circular orbit at an inclination of 83.7° [*Reigber et al.*, 2002]. The initial altitude was ~450 km , and from 2004 to 2005 the altitude descended to ~380 km on average. The orbital period was about 93 min, thus circling the Earth about 15 times per day. The orbital plane precessed at a rate of 1 h in local time per 11 days, resulting in a 24 h of local time coverage within

130 days. The STAR accelerometer aboard CHAMP measures nonconservative forces exerted on the satellite in the along-track and the cross-track directions [*Reigber et al.*, 2002]. From the accelerometer observations the thermospheric zonal wind and air density can be derived in an interactive scheme, which works independently of the instrument orientation in space (for details please refer to *Doornbos et al.* [2010]). In order to cover all 24 h in local times, we examined the zonal winds in sets of 131 days centered on the March Equinox, the June Solstice, the September Equinox, and the December Solstice. These data sets were recorded separately for solar maximum years (2002 and 2003) and solar medium years (2004 and 2005). The data was sorted into bins of longitude (15°) and magnetic local time (1 h). The longitudinal mean value was removed in each local time sector to obtain the longitudinal dependence of the zonal wind. The 50° to 60° MLat ranges in the two hemispheres represent the subauroral regions, which are the focus of the present study.

GITM, which was developed at the University of Michigan, is a three-dimensional model that simulates the ionosphere and thermosphere. A complete description of the model can be found in *Ridley et al.* [2006]. The model solves the continuity, momentum, and energy equations in the thermosphere and ionosphere using realistic source terms. The neutral momentum equation is solved by considering the pressure gradients, ion drag, viscous force, and Coriolis force. GITM is driven by the high-latitude electric field [*Weimer*, 2005], auroral particle precipitation [*Fuller-Rowell and Evans*, 1987], solar EUV, and tides (global scale wave model) at the lower boundary [*Hagan et al.*, 1999]. GITM is initiated by using Mass Spectrometer Incoherent Scatter [*Hedin*, 1991] and International Reference Ionosphere [*Bilitza*, 2001] neutral and ion densities and temperatures. The geomagnetic topology can be described either by the dipole field or International Geomagnetic Reference Field (IGRF) [*Maus et al.*, 2005].

For this study, GITM was run with a resolution of 5° latitude by 10° longitude and with a stretched altitude, resolving the vertical scales with approximately 1/3 of a scale height. It was run for 48 h to reach a quasi steady state. The simulations were continued from the startup simulation for another 24 h before analysis. We simulated the zonal winds in local summer under solar maximum conditions in both hemispheres; this was essential for the development of the middle latitude summer nighttime anomaly (MSNA) [e.g., *Bellchambers*, 1958; *Lin et al.*, 2009; *Liu et al.*, 2009]. Zonal wind patterns in other seasons, while somewhat different from those in summer, were formed by the same mechanisms and thus are not shown. The input parameters were averaged over a length of 131 days centered on 21 June 2002 and 21 December 2002, respectively: interplanetary magnetic field (IMF) $B_x = -0.1$ nT, IMF $B_y = 0.2$ nT, and IMF $B_z = 0.11$ nT; solar wind velocity, $V_x = 567$ km/s, $F_{10.7} = 150$ W/m²/Hz; and hemispheric power, HP = 32.8 GW. The tides at the low boundary are turned off in order to check the in situ physical processes. Moreover, *Wu et al.* [2014b] found that the nonmigrating tidal effects from the low atmosphere were negligible at the United States and Chinese stations for two cases in October 2012.

The realistic run in local summer was set as the base run for comparison with the following simulations: one simulation was performed with the dipole axis aligned with the rotation axis (i.e., tilt angle = 0) to examine the dipole tilt effect; two simulations were conducted using $F_{10.7}$ values of 70 and 100 W/m²/Hz to test the solar EUV flux effects; and four simulations were conducted with enhanced neutral air pressure gradients, zero ion drag, zero viscous force, and zero Coriolis force. These model results were compared with the base run to assess the individual roles of air pressure gradients, ion drag, viscous force, and Coriolis force.

3. Results

3.1. CHAMP Observations

Figures 1 and 2 show the obtained residuals, e.g., the differences in zonal winds (ΔUy), in the frame of the magnetic local time (MLT) and geographic longitude during solar maximum and medium years. The longitudinal mean value was subtracted for each MLT hour to give the ΔUy, which is dependent on MLT. From top to bottom are displayed March Equinox, June Solstice, September Equinox, and December Solstice results. Figures 1 and 2 (a, c, e, and g) are from the Northern Hemisphere, and Figures 1 and 2 (b, d, f, and h) are from the Southern Hemisphere. Positive velocities of zonal wind point in the eastward direction. We observed a prominent wave-1 structure (i.e., one peak and trough) in the longitudinal profile, with its phase in the Northern Hemisphere opposite to that in the Southern Hemisphere. The phase of the wave pattern reversed over the course of a day. During the nighttime ΔUy appeared as a positive deflection in eastward direction within the longitude sector from 90°W to 90°E and a negative deflection in westward direction outside of that sector; during the daytime ΔUy appeared as a negative deflection within the longitude sector from 90°W to 90°E and a positive one otherwise. This situation was reversed in the Southern Hemisphere: a negative deflection was
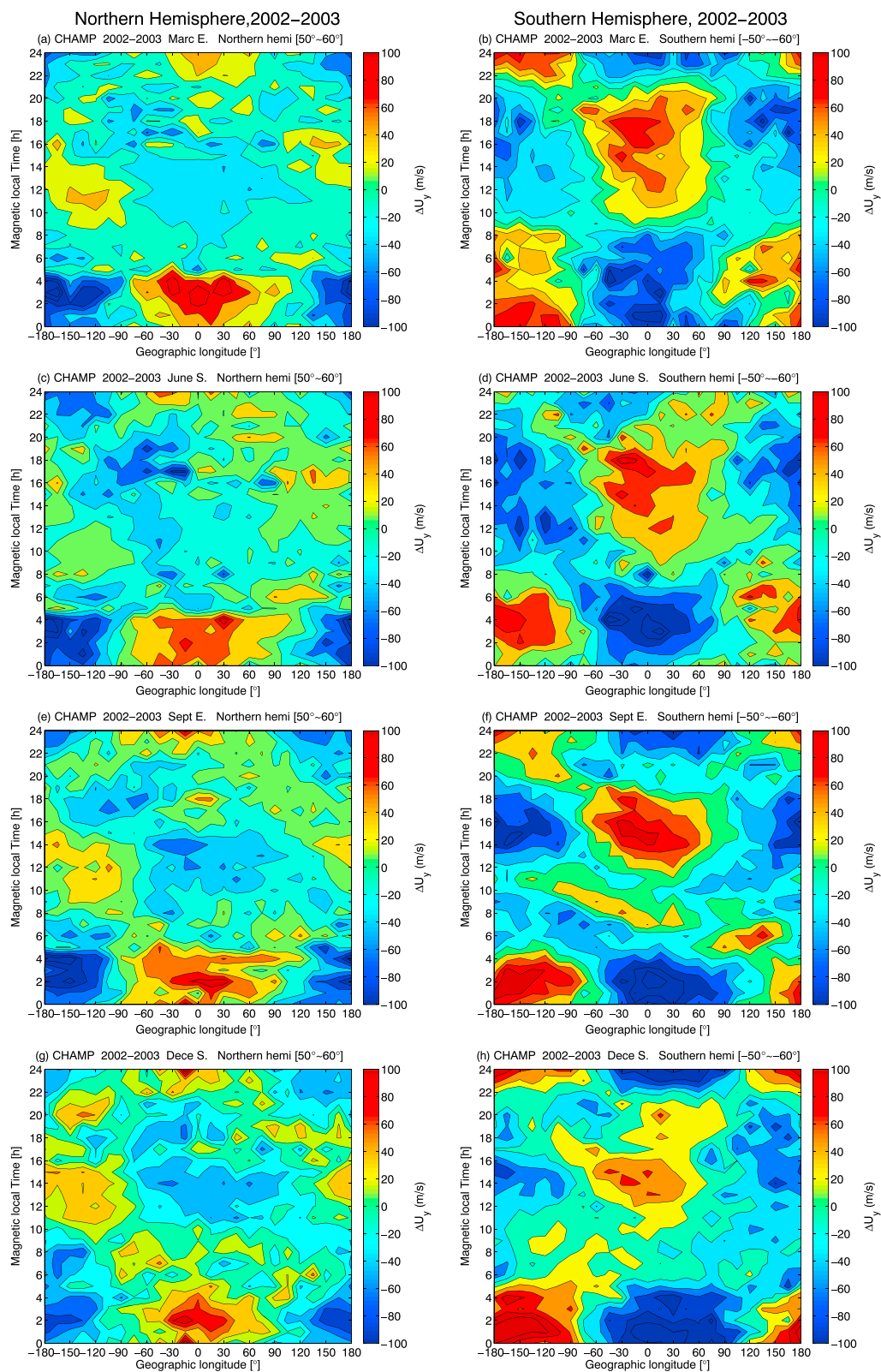
Figure 1. Geographic longitudinal versus magnetic local time variations of the difference in the zonal wind at 50°–60° MLat in the (a, c, e, and g) Northern Hemisphere and (b, d, f, and h) Southern Hemisphere during years of 2002 and 2003, as observed by CHAMP. From top to bottom are results from March Equinox, June Solstice, September Equinox, and December Solstice.
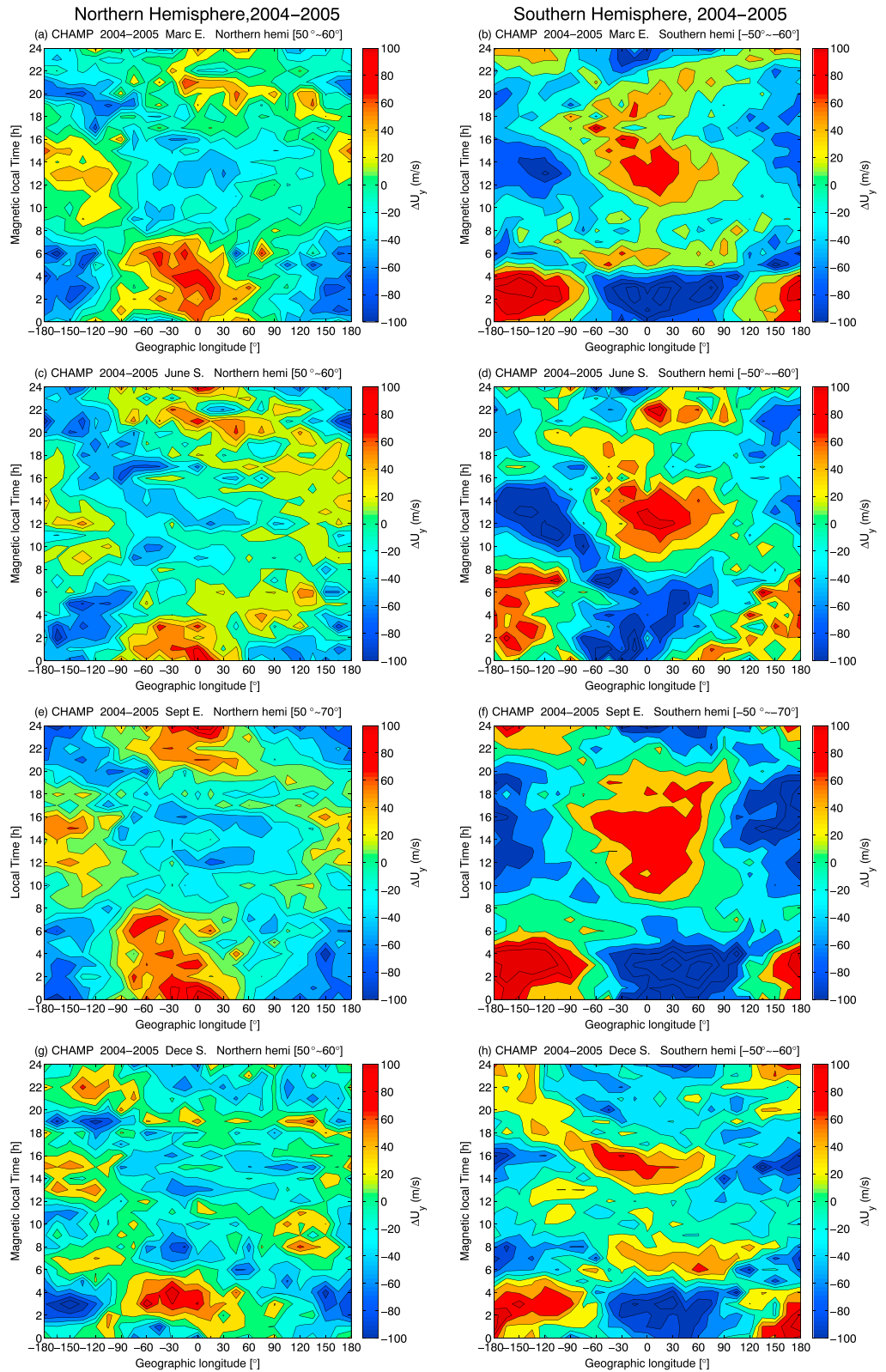
Figure 2. Same format as Figure 1, but from years of 2004 and 2005.

Table 1. Peak West-East Differences of Zonal Wind Speed Observed by CHAMP for Both Daytime and Nighttime During Solar Maximum Years of 2002–2003[a]

	Northern Hemisphere		Southern Hemisphere	
	Daytime (m/s)	Nighttime (m/s)	Daytime (m/s)	Nighttime (m/s)
MarcE	118 (107)	286 (194)	194 (209)	208 (315)
JuneS	172 (119)	284 (180)	181 (225)	276 (255)
SeptE	125 (121)	257 (205)	260 (221)	300 (392)
DecsS	112 (170)	212 (252)	179 (227)	309 (261)

[a]The values in parenthesis are from solar medium years of 2004–2005.

observed from 90°W to 90°E during the nighttime, while it was positive during the daytime. Such a wave-1 pattern persisted for the whole year and for two solar activity levels. The shift from nighttime to daytime patterns occurred later in local time during local winter as compared to summer. For example, the shift occurred around 10 MLT at December Solstice and around 6 MLT at June Solstice at solar maximum in the Northern Hemisphere, as compared to 6 MLT and 8 MLT, respectively, in the Southern Hemisphere.

The peak west-east differences of ΔUy were calculated for both the daytime and nighttime and were listed in Table 1. The peak differences of the positive and negative deflections were calculated separately for daytime and nighttime. The peak west-east differences of ΔUy at nighttime tended to occur in the postmidnight sector, while values at daytime tended to occur in the afternoon. Regardless of the season and solar activity, the nighttime peak west-east differences of ΔUy were usually larger than the daytime values in both hemispheres. In local summer and winter, the peak west-east differences of ΔUy were usually larger in the Southern Hemisphere than in the Northern Hemisphere, which is more obvious under solar medium conditions than under solar maximum conditions.

3.2. GITM Model Runs

To investigate the production mechanism of the prevailing wave-1 pattern of the zonal winds, the ionosphere and thermosphere systems in local summer under solar maximum conditions were simulated by the GITM model in both hemispheres. As mentioned above, the summer winds are closely related to the MSNA. The simulated contours of ΔUy at an altitude of 400 km in both hemispheres are depicted in Figure 3 in the frame of GLon versus MLT: each figure uses the same contour intervals and color scale.

At middle latitudes, the F region zonal winds are produced mainly by the pressure gradients caused by the day-night differences in solar heating. In addition, the zonal wind patterns are affected by the ion drag, viscosity, and Coriolis force [*Richmond et al.*, 2003]. The zonal wind momentum equation can be expanded in the spherical coordinate system as follows:

$$\frac{\partial u_\phi}{\partial t} + u_r\frac{\partial u_\phi}{\partial r} + \frac{u_\theta}{r}\frac{\partial u_\phi}{\partial \theta} + \frac{u_\phi}{r\cos\theta}\frac{\partial u_\phi}{\partial \phi} = -\frac{1}{\rho r\cos\theta}\frac{\partial P}{\partial \phi} + \frac{F_\phi}{\rho} + \frac{u_\phi u_\theta\tan\theta}{r} - \frac{u_r u_\phi}{r} + 2\Omega u_\theta\sin\theta - 2\Omega u_r\cos\theta \quad (1)$$

$$F_\phi = \rho_i v_{in}(v_\phi - u_\phi) + \frac{\partial}{\partial r}\eta\frac{\partial u_\phi}{\partial r} \quad (2)$$

where u_ϕ, u_r, u_θ are zonal, radial, and meridional wind components, r, θ, ϕ are radius, latitude, longitude in spherical coordinate systems, ρ is mass density, and P is neutral air pressure. F_ϕ are ion drag and viscosity force in the ϕ direction (see equation (2)), where ρ_i is ion density, v_{in} is collision frequency, v_ϕ is ion velocity in eastward direction, and η is the coefficient of viscosity. The first term in F_ϕ is ion drag, and the second term is viscosity force due to the radial shear of the horizontal wind. The last two terms in equation (1) are due to Coriolis force and Ω is the Earth's angular velocity.

In the following, we investigated various physical factors that might modulate the longitudinal distribution of the zonal wind, including magnetic field geometry, pressure gradient, ion drag, viscous force, and Coriolis force.

3.3. Geomagnetic Field Geometry

For Figures 3a and 3b we considered the presence of an IGRF magnetic field configuration with nonzero tilt, while for Figures 3c and 3d the results were from runs using a centered dipole field with zero tilt
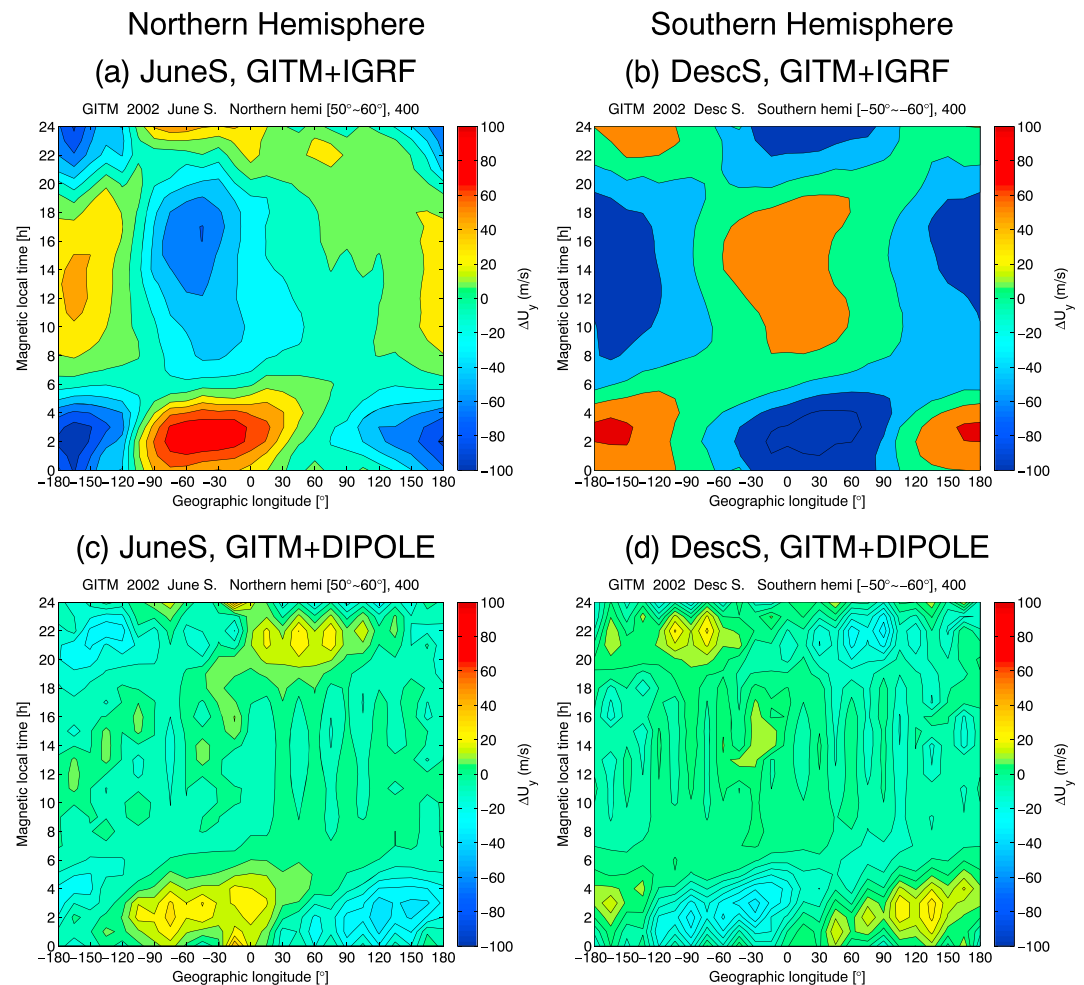
Figure 3. Geographic longitudinal versus magnetic local time variations of the difference in zonal wind simulated by GITM for local summer seasons at 50°–60° MLat in the (a and c) Northern and (b and d) Southern Hemispheres. For Figures 3a and 3b we used a realistic IGRF geomagnetic field (base run), while Figures 3c and 3d are based on a centered dipole field with zero dipole tilt.

(i.e., magnetic pole was aligned with the geographic pole). The IGRF case was the base run; in it there was generally good agreement between the model (Figures 3a and 3b) and observations of large-scale structures (Figures 1c and 1h). Both the model and the experimental results showed a prominent wave-1 structure in the longitudinal profile, which were opposite in phase in the Northern and Southern Hemispheres. The peak longitudinal differences of the simulated ΔUy speeds were determined for daytime and nighttime, as was done for the CHAMP observations. The peak differences for daytime and nighttime in both hemispheres simulated for summer conditions are all listed in Table 2. The quantities of these base runs are used for comparison with subsequent simulation results. The peak longitudinal differences of ΔUy at nighttime were larger than those at daytime and larger in the Southern Hemisphere than in the Northern Hemisphere. The local time and hemispheric asymmetries of the peak differences were consistent with CHAMP observations.

The present work aims to compare the model with observed results in qualitative ways, not in quantitative ways. The model presented a 1 day result driven by solar wind and IMF parameters averaged over 131 days periods, while the satellite observations were an accumulation of 131 days. Thus, it was not surprising that the modeled amplitudes and spatial distributions were not exactly the same as the observations. The model underestimated the observed longitudinal differences of the zonal wind ΔUy, which was presented in Tables 1 and 2. However qualitatively, the model reproduced the main longitudinal and diurnal features of the zonal wind well, which was at the focus of the presented work. This affirmed that the model could be used to investigate the generation mechanism of the prevailing wave-1 pattern of the zonal winds.

Table 2. Peak West-East Differences of Zonal Wind From GITM Simulations for Both Daytime and Nighttime at Local Summer[a]

	Northern Hemisphere (JuneS)		Southern Hemisphere (DescS)	
	Daytime (m/s)	Nighttime (m/s)	Daytime (m/s)	Nighttime (m/s)
Base run(IGRF)	109	199	178	240
Dipole run	26	70	26	59
PG run	117	243	192	323
IDoff run	131	178	187	289
VFoff run	156	214	254	229
CFoff run	128	229	190	261
$F_{107}100$	84	160	118	187
$F_{107}70$	63	123	83	140

[a]From top to bottom are six runs with IGRF, dipole field, enhanced neutral pressure gradient (PG), Ion drag off (IDoff), Viscous force off (VFoff), and Coriolis force off (CFoff). These cases are under solar maximum condition with $F_{10.7}$ of 150. The last two cases are under solar medium and minimum conditions with $F_{10.7} = 100$ and 70.

In the simulation with zero dipole tilt, ΔUy diminished at daytime, while they were present with weaker amplitudes at nighttime (see Figures 3c and 3d). ΔUy values in the premidnight sector were opposite to those in the postmidnight and in the Northern and Southern Hemispheres. Compared to the base run with its nonzero tilt, the zonal speed differences with zero dipole tilt were reduced by about 65%–85% (see Table 2). This indicates that the displacement between the magnetic pole and the geographic pole or dipole tilt is crucial for the longitudinal differences of the zonal wind. The reasons for these discrepancies are discussed in more details in section 4.

3.4. Pressure Gradient
The absorption of EUV solar radiation is a major heat source for the thermosphere. The day-night pressure gradients account for most of the middle latitude zonal wind patterns. To determine how pressure gradients affect ΔUy, the pressure gradient term in the neutral momentum function was artificially enhanced by a factor of 5; this was termed as the "PG run." Figures 4a and 4b show the simulated ΔUy with increased pressure gradients. The longitudinal structures of ΔUy were quite similar in structure to the base run, except that the magnitudes of the differences were enhanced. The effects of the pressure gradients are more clearly presented in Figures 4c and 4d, where the residual ΔUy (PG run — base run) are shown. The residuals of ΔUy in particular were caused by the enhanced pressure gradients, which were similar in structure to those shown in Figures 4a and 4b. The enhancements were more obvious at nighttime than at daytime, which indicates that the pressure gradients improve the model results with respect to the observed wave-1 pattern of the zonal wind.

3.5. Ion Drag
In the F region the neutral motion can be altered by the collisions with ions. At middle latitudes the collision between the neutral gas and the oxygen (O$^+$) ions provides a retarding force for zonal winds during quiet periods. This is called the ion drag effect. To examine the ion drag effect on ΔUy, we performed a simulation by turning off the ion drag in the model. Figures 5a and 5b show the "IDoff run," which simulated ΔUy in both hemispheres when the ion drag was removed. The local time and longitudinal variations of ΔUy were quite similar to the base run shown in Figures 3a and 3b, although the centers of the peak and trough shifted eastward at nighttime and westward at daytime. The nighttime peak ΔUy in the Northern Hemisphere shifted to the premidnight sector, which was in the postmidnight sector in the base run. The differences in ΔUy between the IDoff run and base run, which were caused by the ion drag effect, are shown in Figure 5c and 5d. Ion drag had the greatest effect at nighttime showing almost opposite variations to Figures 5a and 5b. This indicates that ion drag reduces the compatibility between the modeled and observed longitudinal variations in zonal winds.

3.6. Viscous Force
The horizontal winds at different altitudes are coupled together through frictional drag, which is also known as viscous force. To assess the effect of viscous force on ΔUy, we performed a "VFoff run" in which the viscous force was excluded. The diurnal and longitudinal variations of the simulated ΔUy are shown in Figures 6a and 6b, and the residual ΔUy (base run — VFoff run) is shown in Figures 6c and 6d. The wave-1 longitudinal
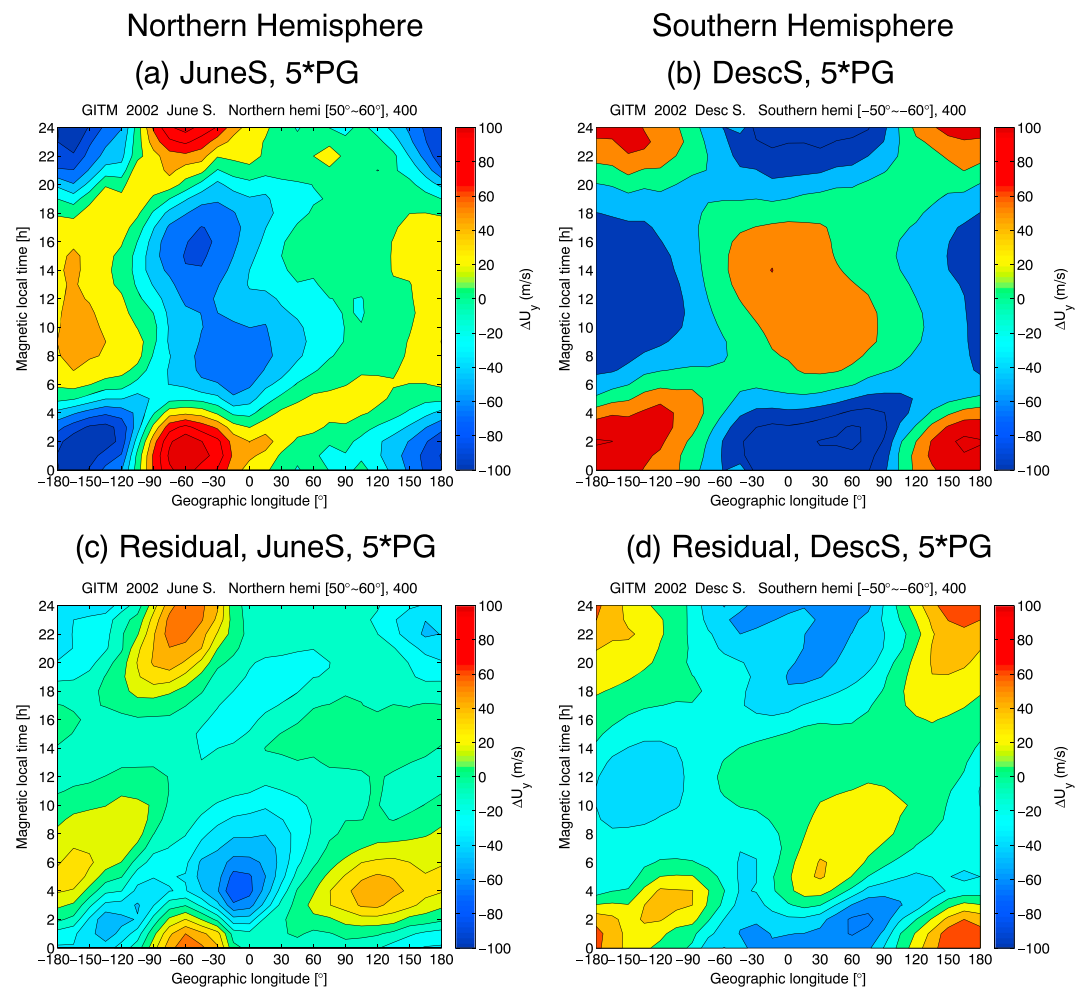
Figure 4. (a–b) Geographic longitudinal versus magnetic local time variations of the difference in the zonal wind (ΔUy) at 50°–60° MLat as simulated by GITM when the pressure gradient (PG) was enhanced by a factor of 5. (c–d) Residual Uy (PG run - base run) due to the enhanced pressure gradients.

pattern of ΔUy was similar to the base run. The residual ΔUy (Figures 3c and 3d) varied in nearly opposite ways to the base run. This means that the viscous force also reduces the compatibility between the modeled and observed longitudinal pattern of the zonal wind.

3.7. Coriolis Force

The Coriolis force is an important factor for zonal winds at middle latitudes. The equatorward meridional winds resulting from the high-latitude Joule heating are propagated to the middle latitude and turned westward due to the Earth's rotation; poleward winds are similarly turned eastward. To assess the Coriolis effect on ΔUy, we conducted a CFoff run in which we turned off the Coriolis force in the model. Figures 7a and 7b show the simulated ΔUy along with the residual ΔUy (base run — CFoff run) in Figures 7c and 7d. Again, similar wave-1 patterns of ΔUy were found for runs with and without the Coriolis force. The changes in the residual ΔUy due to the Coriolis force were generally weaker than those caused by ion drag and viscous force. The Coriolis force improves the modeled with respect to the observed ΔUy around midnight, while it tends to reduce the compatibility between modeled and observed ΔUy at daytime.

4. Discussion

We have studied the longitudinal variation of zonal winds at subauroral regions from a global perspective. Based on CHAMP observations, we have found that these zonal winds show obvious wave-1 variations along the longitude and that these reverse in phase over the whole day and in both the Northern and Southern Hemispheres. Such prominent longitudinal and diurnal variations persist throughout the whole
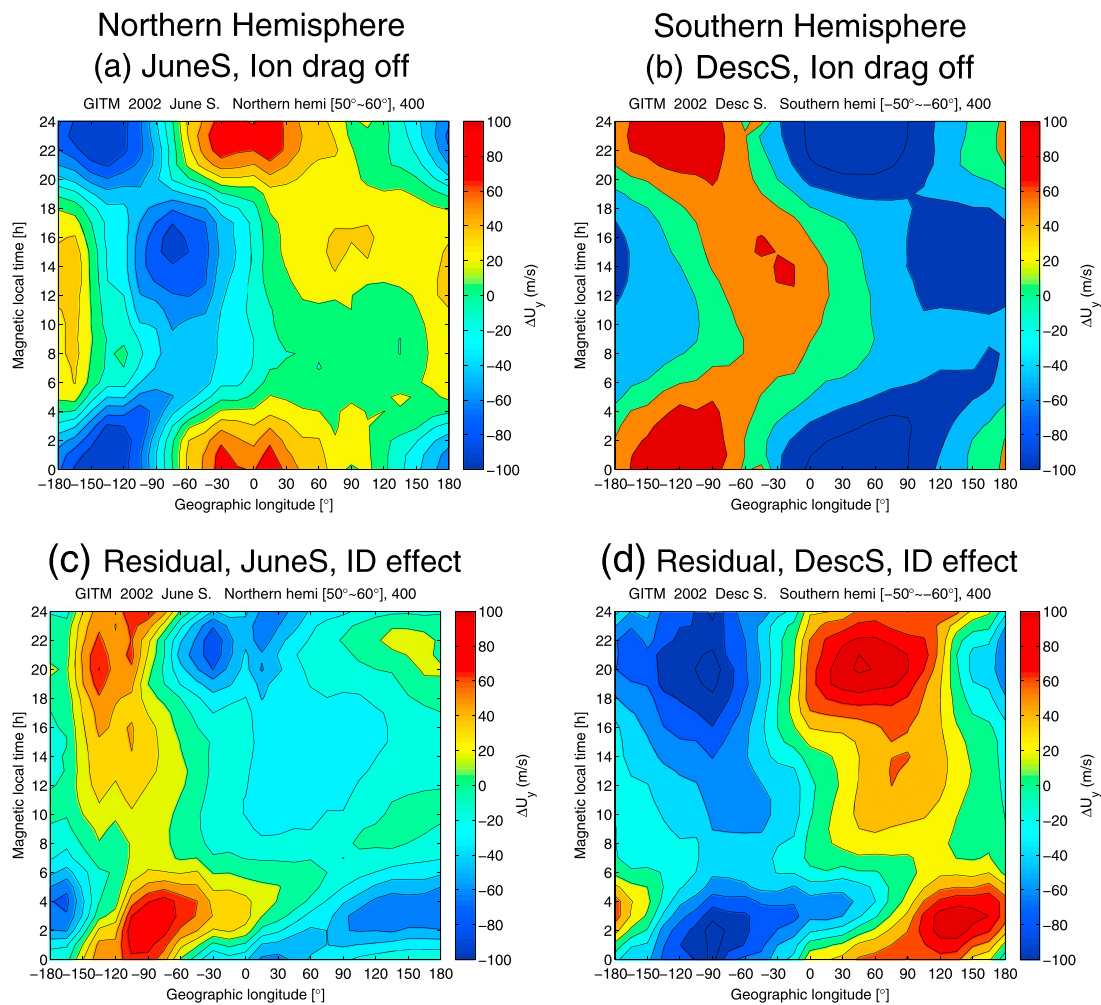
Figure 5. (a–b) Geographic longitudinal versus magnetic local time variations of the difference in the zonal wind at 50°–60° MLat as simulated by GITM when the ion drag was turned off. (c–d) Residual *Uy* (base run - IDoff run) due to the ion drag. Figure 5 (a-d) title font size is smaller as compared to Figure 3, 4, 6 et al.

year, regardless of the solar activity. The nightside differences were larger than those of the dayside, and the longitudinal differences in the south were larger than those in the north.

Wu et al. [2014b] compared the western and eastern hemispheric zonal winds at nighttime based on three FPI observations in North America and China. They reported that the nighttime zonal winds were very similar at the Boulder (105°W GLon) and the Xinglong (112°E GLon) and the Kelan (115°E GLon) stations in October 2012. The CHAMP map of zonal winds at the September Equinox (Figures 1e) shows that the zonal winds at Boulder and XingLong/KeLan were deflected in the same direction: negative at nighttime and positive at daytime. Prominent longitudinal differences should exist between longitudinal bands from 90°W to 90°E and 180°W to 90°W, 90°E to 180°E. *Wu et al.* [2014b] noticed that near dawn the Boulder westward wind was about 50 m/s stronger than the eastern data (Figures 3 and 4). In CHAMP map, Δ*Uy* changed direction from westward to eastward in the early morning, which was a little earlier at 110°E GLon than at 105°W GLon.

As introduced in section 1, several previous works concentrated on the local time, seasonal, solar, and magnetic activity variation of the zonal wind. However, the mechanisms for the longitudinal variation of the zonal wind were not fully investigated. By using the global ionosphere and thermosphere model, the present work focuses on the physical effects for the first time, which may be responsible for the longitudinal modulation of the zonal wind.

4.1. Geomagnetic Field Geometry
The simulations with IGRF were more consistent with the observations when compared to those with the centered dipole field (see Figure 3). This indicates that the actual geomagnetic field configuration is crucial for
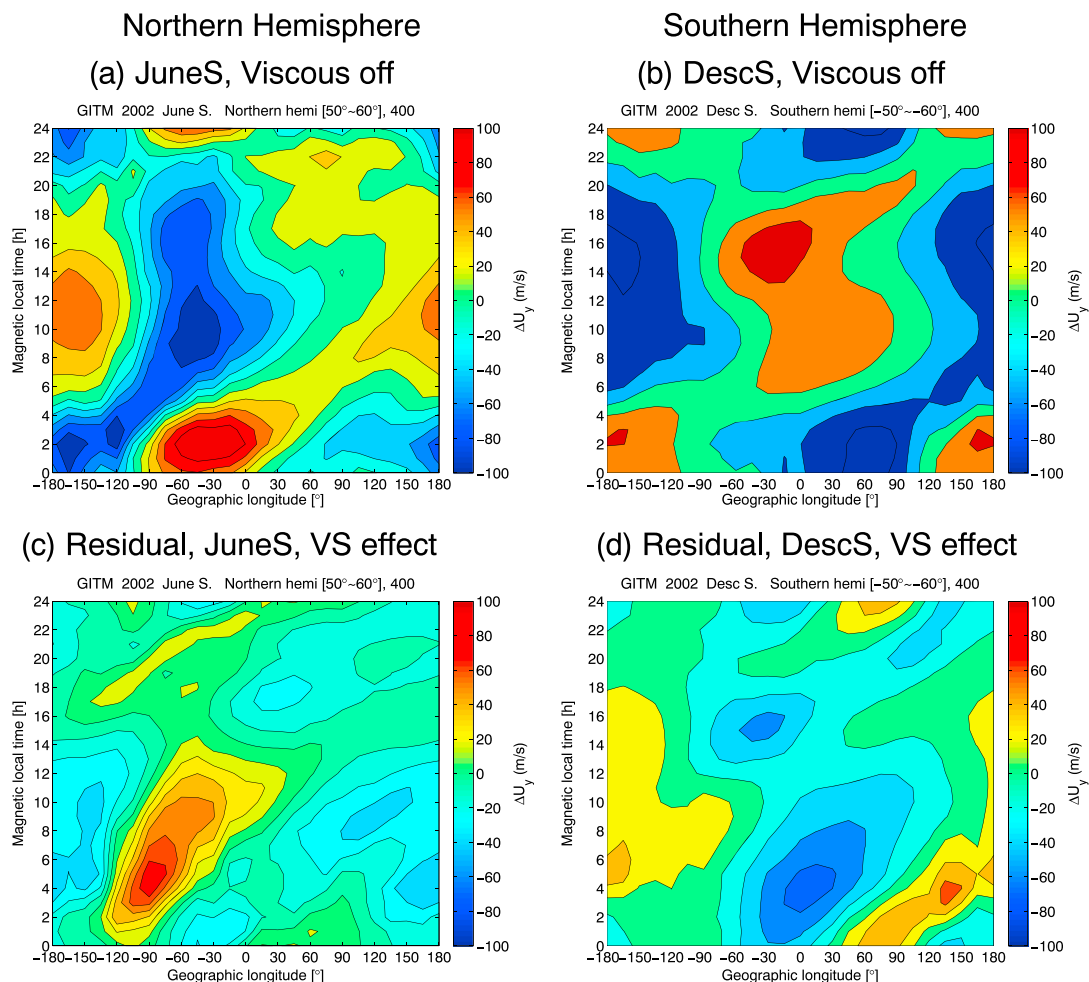
Figure 6. Same format as Figure 5, but for the case when viscous force is turned off.

the longitudinal differences in zonal winds. Due to the magnetic axis tilt, the geomagnetic and geographic coordinates are different from each other. Along the same magnetic latitudinal bands the geographic latitudes vary with longitude depending on their distance from the magnetic poles. This causes longitudinal differences in the pressure gradient and Coriolis force, both of which are depending on geographic latitudes. Subsequently, longitudinal differences in zonal winds can occur.

Interestingly, the model showed that with a zero-tilt dipole field, there were still small ΔUy amplitudes predominantly at nighttime. These are obviously not caused by the pressure gradient, as geographic and geomagnetic coordinate systems are the same. Therefore, no longitudinal difference of solar heating is expected. When examining the longitudinal difference of the ion velocity (figure not shown), we found that the ΔUy were similar to the ion velocity. Thus, we conclude that ion drag is the main factor affecting ΔUy in the dipole field.

Cnossen and Richmond [2012] examined the dipole tilt effect for the magnetosphere-ionosphere system by using the Coupled Magnetosphere-Ionosphere-Thermosphere model with a 0° and a 30° dipole tilt. Their Figure 6 showed the global map of 24 h averaged zonal winds for 0° and 30° tilt, in which the longitudinal difference was negligible for the zero tilt. This was inconsistent with our result revealing longitudinal differences exist at nighttime due to the ion drag effect (see Figures 3c and 3d). When averaged over 24 h, the ion drag effect canceled itself out, so that its influence on the neutral wind became small. In *Cnossen and Richmonds*, [2012, Figure 6], for a 30° tilt, the 24 h averaged zonal winds showed weaker westward winds around 60°W–60°E and stronger westward winds at other longitudes. Since the nighttime variations were larger than the daytime ones, as shown by both CHAMP and GITM results, the 24 h averages should have reflected the nighttime pattern: in this sense their results were consistent with our results.
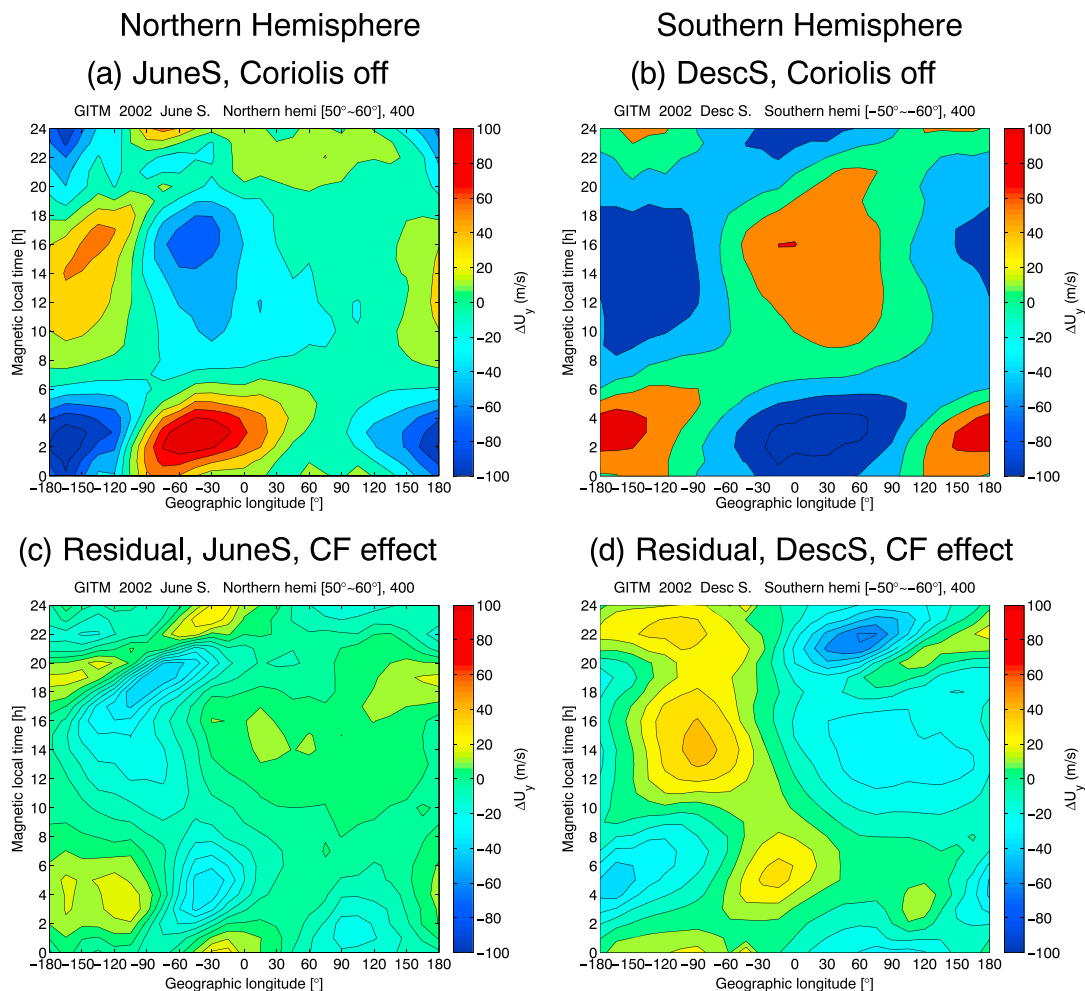
Figure 7. Same format as Figure 5, but for the case when the Coriolis force is turned off.

4.2. Pressure Gradient

It is known that the zonal winds at middle latitudes largely reflect the global circulation pattern set up by the neutral air pressure gradients induced by the solar EUV heating. However, the longitudinal effects of the air pressure gradient have not been investigated previously. Our results indicated that with enhanced pressure gradients, the longitudinal differences of the zonal wind increased in magnitudes. This suggests that the pressure gradient improves the model results with respect to observed ΔUy.

The neutral air pressure is $P = nkT = \frac{k}{m}\rho T$, where n is the number density, k is the Boltzmann constant, T is the neutral temperature, m is the average mass of the neutral particles, and ρ is the mass density. The azimuthal pressure gradient term in equation (1) can be expressed as

$$\frac{1}{r\cos\theta}\frac{1}{\rho}\frac{\partial P}{\partial \phi} = \frac{1}{r\cos\theta}\frac{k}{m}\left(\frac{T}{\rho}\frac{\partial \rho}{\partial \phi} + \frac{\partial T}{\partial \phi}\right) \tag{3}$$

Both air density and temperature gradients contribute to the air pressure gradient. Figure 8 shows the longitudinal differences of mass density, $\Delta\rho$, and neutral temperature, ΔTn. Both $\Delta\rho$ and ΔTn showed wave-1 variations along longitude, which reversed in phase throughout the day. The longitudinal differences of gradients of ρ and Tn showed quite similar structures to those patterns of ΔUy in Figures 4c and 4d.

One of the candidates causing the longitudinal differences in air density and temperature is the intensity of solar illumination, which can be represented by the solar zenith angle (SZA). Figures 9a and 9b show the longitudinal and diurnal variations of ΔSZA along our magnetic latitude band based on IGRF. A positive value means larger SZA (i.e., less sunlight) with respect to the longitudinal mean. The overlayed white line
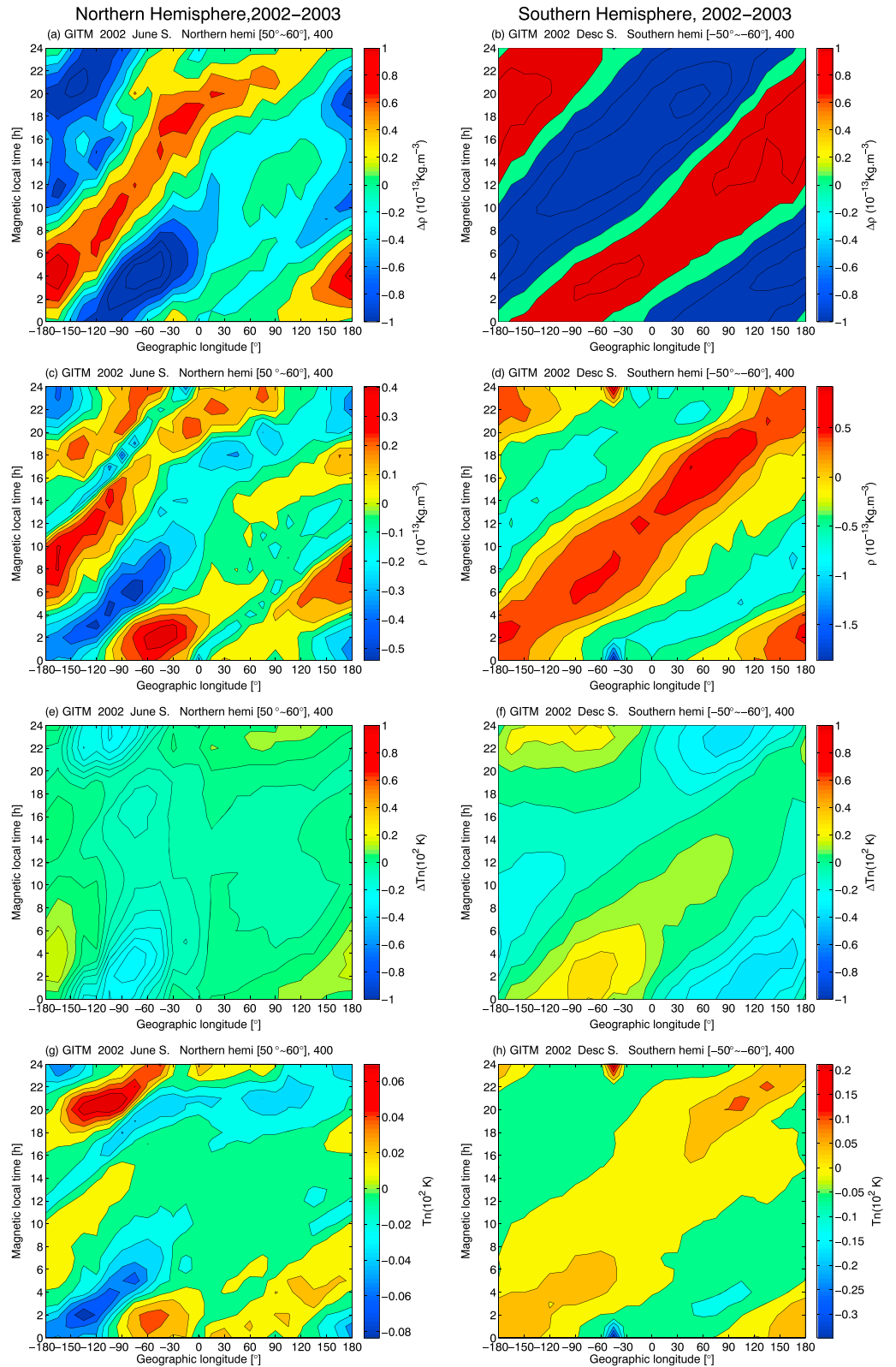
Figure 8. Geographic longitudinal versus magnetic local time variations of the difference in the air density ($\Delta\rho$, a–b), neutral temperature (ΔTn, c–d), and their gradient in the local time direction (ρ gradient, c–d, Tn gradient, g–h).
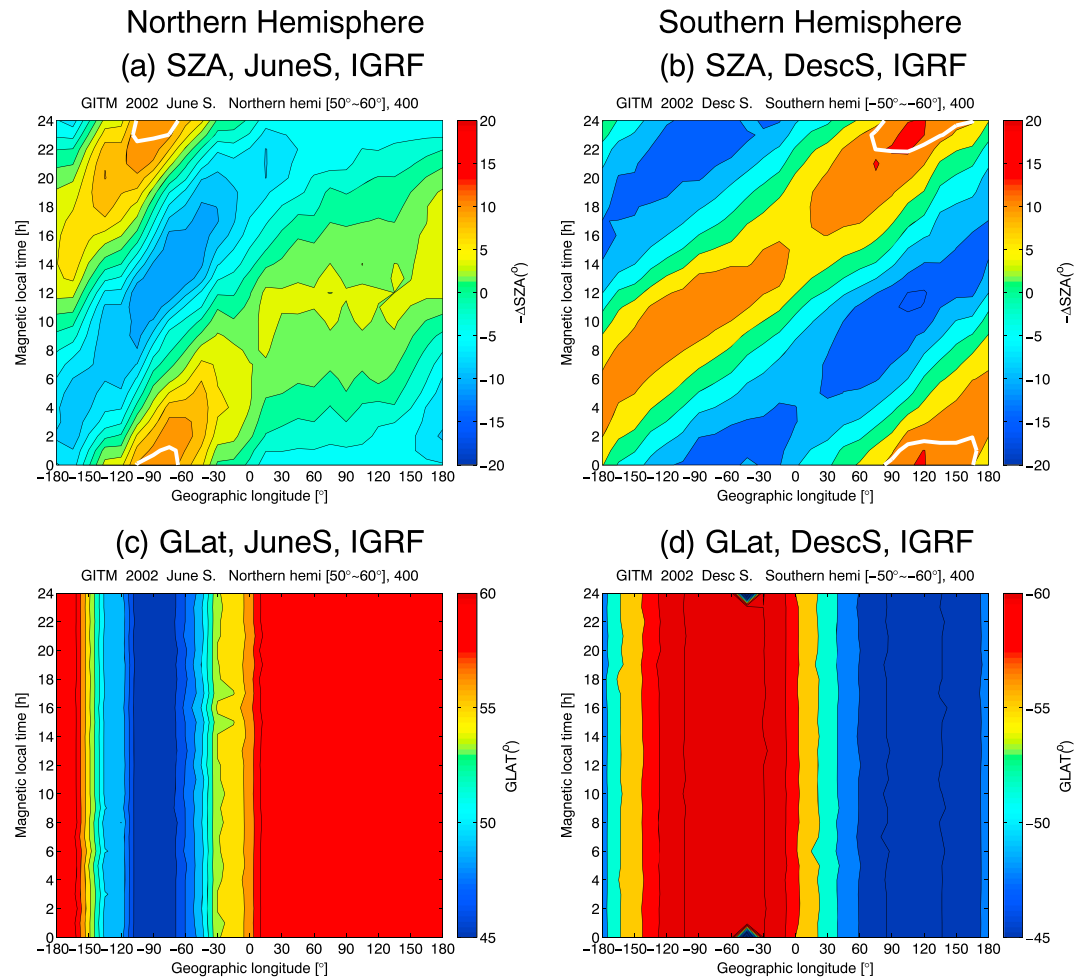
Figure 9. (a–b) Geographic longitudinal versus magnetic local time variations of the difference in the solar zenith angle (Δ*SZA*). Over-plotted white lines indicate the solar terminator position (*SZA* = 100°) for the IGRF magnetic field case. (c–d) Geographic longitudinal versus magnetic local time variations of the geographic latitude (*GLat*) covered by our latitude band.

indicates the terminator (i.e., SZA = 100°), which separates the illuminated dayside from the dark nightside [*Wang et al.*, 2005].

Within the IGRF frame, longitudinal variations of the solar illumination existed, because our magnetic latitude band followed different geographic latitudes around the globe. ΔSZA showed a wave-1 structure along the longitude profile in both hemispheres, which were similar to those of mass density and temperature (Figures 8a and 8b and 8e and 8f). The longitudinal sectors (90°W and 120°E) hosting the north and south magnetic poles coincided with strongest perturbations. Figures 9c and 9d showed the geographic longitudinal variations along our magnetic latitude bands from ±50 to ±60°. In the two hemispheres the resulting geographic latitude was lowest on longitudes hosting the magnetic poles and largest 180° in longitudes apart. The differences in geographic latitude were the reason for the longitudinal dependence of the SZA. Consequently, both mass density and neutral temperature were expected to show obvious longitudinal variations in response to solar illumination. From Figure 9 one can notice that the solar illumination effect in the Southern Hemisphere was larger than that in the Northern Hemisphere. This can explain the fact that the longitudinal dependence of the mass density and neutral temperature were larger in the south than in the north.

This idea is further supported by the $F_{10.7}$ dependence of Δ*Uy*. We have changed the $F_{10.7}$ value from 150 in the base run to values of 100 and 70 for solar medium (years 2004–2005) and minimum conditions, respectively. The residual Δ*Uy* are shown in Figure 10 (base run—$F_{10.7}$ run). These residuals showed patterns similar to the base run, as was observed in Figures 3a and 3b. Δ*Uy* increased in magnitude as $F_{10.7}$ increased.
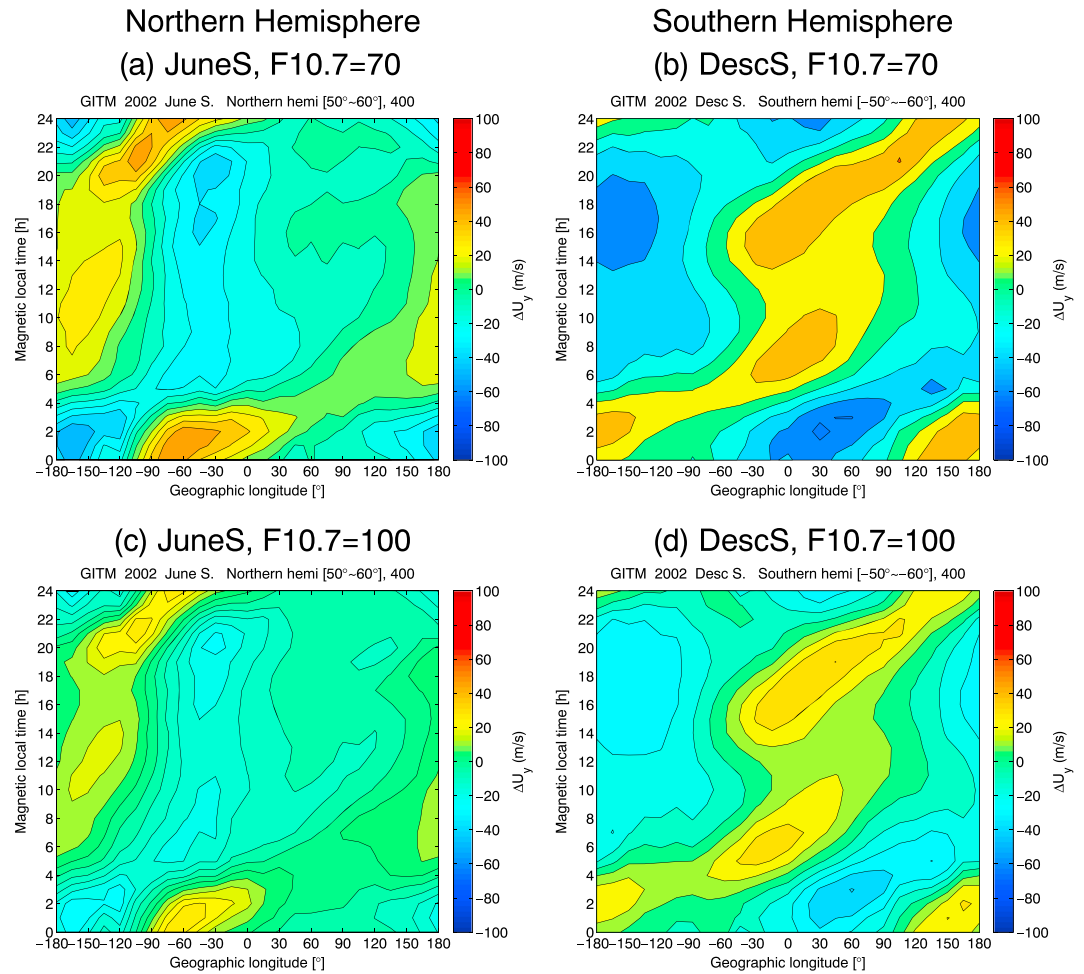
Figure 10. Residual ΔUy (base run—$F_{10.7}$ run) due to solar flux $F_{10.7}$ effects. (a and b) $F_{10.7} = 70$ and (c and d) $F_{10.7} = 100$.

This indicates the dominant role of the solar EUV heating in the longitudinal pattern of zonal winds in the model and supports the proposed theory that pressure gradient plays an important role in the longitudinal modulation of the zonal wind at subauroral latitudes.

Figure 11 shows the peak longitudinal differences of ΔUy in local summer for both the daytime (red) and nighttime (black) in the Northern (circle) and Southern (asterisk) Hemispheres as a function of $F_{10.7}$. The GITM results are shown as dashed line, while the CHAMP results are as solid line. As predicted by the model, larger $F_{10.7}$ values provided a stronger correlation with ΔUy. The peak longitudinal differences increased with $F_{10.7}$, and there was a saturation (weakening) effect when $F_{10.7}$ was greater than 100. CHAMP results have solar cycle trends that were similar to GITM results but with larger amplitudes; an exception made the daytime in the Southern Hemisphere, when the peak difference seemed to decrease under solar maximum conditions. The increased ion drag at solar maximum might win over the increased pressure gradient under those conditions [*Emmert et al.*, 2006]. *Kawamura et al.* [2000] found that the pressure gradients were greater at solar maximum, but the driving force was $\frac{1}{\rho}\frac{\partial P}{\partial \phi}$ (see equation (1)), and so the increase in pressure gradient might be compensated by the accompanying increase in density. The differences between model and observations indicate that the GITM overestimates the relative roles of the pressure gradient effect at daytime in the Southern Hemisphere under solar maximum conditions.

4.3. Ion Drag

The ion drag force, $\frac{\rho_i v_{in}(v_\phi - u_\phi)}{\rho}$ (see equations (1) and (2)), is the major retarding force in the F region, where the movement of ionization is constrained by the Earth's magnetic field. The collisions between the neutral gas and O^+ ions are proportional to the neutral-ion velocity differences ($v_\phi - u_\phi$) and the ion density while
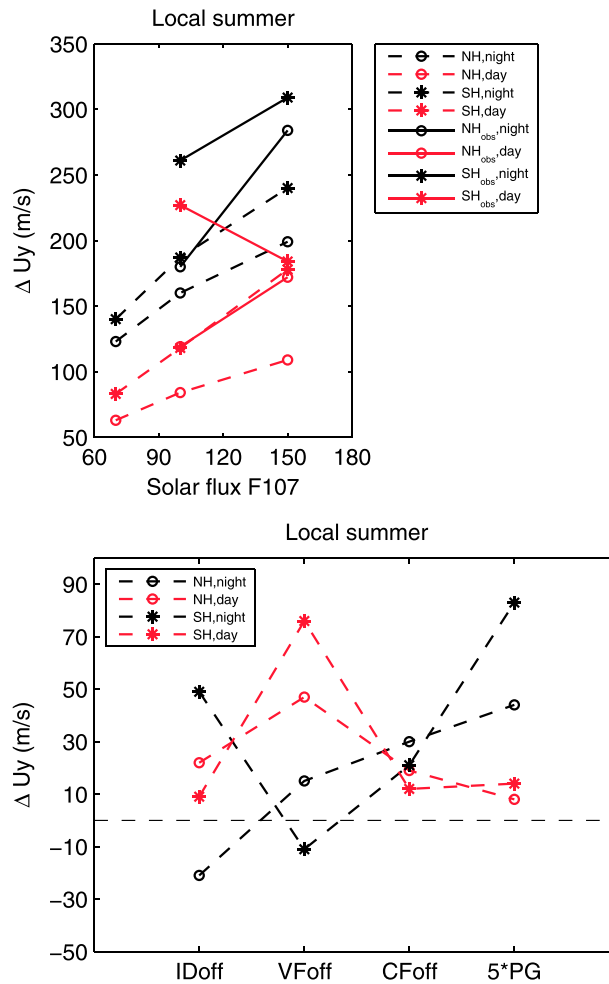
Figure 11. (top) Peak longitudinal differences of ΔUy as a function of $F_{10.7}$ for both daytime and nighttime in the two hemispheres. CHAMP results are in solid lines and GITM are in dashed lines. (bottom) The differences in ΔUy speed between the base run and various runs with ion drag off (IDoff), Viscous force off (VFoff), Coriolis force off (CFoff), and 5 times of pressure gradient (5*PG). The wind data from these runs are all listed in Table 2. The daytime results are shown in red and nighttime in black. The Northern Hemisphere is marked by circle and the Southern Hemisphere by asterisk.

inversely proportional to the neutral density ρ. During quiet periods, v_ϕ is typically smaller than u_ϕ at sub-auroral latitudes ($v_\phi - u_\phi \simeq -u_\phi$). The ion drag acts as a true drag and is approximately proportional to the zonal wind velocity. As expected, the longitudinal variation of the ion drag (see Figures 5c and 5d) generally resembled that of zonal wind (see Figures 5a and 5b) but with opposite phase.

4.4. Viscous Effect
The horizontal winds at different heights are coupled through the frictional drag, which is proportional to η/ρ (see equations (1) and (2)), where the viscosity coefficient η is approximately constant. The mean gas density ρ decreases exponentially with height, resulting in an increase in viscous drag with altitude. The influence of wind forcing from upper levels on lower levels could be considered to be large, since it is inversely proportional to the mass densities at the two levels.

Based on data from GITM simulations, the longitudinal differences of zonal winds increased with increasing altitudes (figures not shown). When the viscous drag effects were turned off, the longitudinal differences of the zonal wind increased at the upper levels. This indicates that the longitudinal differences of the zonal wind is mainly induced in situ in the upper thermosphere, rather than from the lower thermosphere.

4.5. Coriolis Force
The term of the Coriolis force, $\simeq 2\Omega u_\theta \sin\theta$ (see last two terms in equation (1) and assuming negligible vertical neutral wind during quiet periods) is important at high and middle latitudes and negligible at the equator

Table 3. The Amplitudes and Phases Of Diurnal Tidal Components D0 and DW2 of Zonal Winds at 400 km Altitude During Solar Maximum Years of 2002–2003[a]

| | Northern Hemisphere | | | | Southern Hemisphere | | | |
| | D0 | | DW2 | | D0 | | DW2 | |
	Amplitude (m/s)	Phase (h)	Amplitude (m/s)	Phase (h)	Amplitude (m/s)	Phase (h)	Amplitude (m/s)	Phase (h)
MarcE	21.5 (11.7)	0.8 (2.0)	25.7 (18.4)	2.4 (2.9)	14.3 (12.6)	14.9 (12.8)	20.4 (11.7)	16.5 (15.0)
JuneS	*10.3 (15.7)*	*1.7 (0.9)*	14.5 (20.6)	1.7 (23.9)	16.9 (14.2)	16.1 (15.1)	18.1 (16.5)	16.6 (15.95)
SeptE	21.5 (15.6)	1.1 (2.7)	27.2 (25.8)	1.9 (1.0)	16.2 (18.7)	13.0 (13.5)	19.1 (19.3)	13.7 (17.0)
DecsS	17.2 (6.1)	2.1 (3.1)	18.9 (6.7)	2.9 (1.8)	*40.1 (15.8)*	*12.8 (12.5)*	*32.6 (19.2)*	*15.1 (13.1)*
GITM	23	2.9	30	0.9	22	13.7	18	5.1

[a]The values in parenthesis are from solar medium years of 2004–2005. The values from local summer are in italic for comparison with the model. The GITM results are listed in the last row, which is from local summer in the two hemispheres.

as $\sin\theta = 0$. The equatorward wind will deflect westward, and the poleward wind will deflect eastward due to the Earth's rotation. The longitudinal difference of the Coriolis force came from both the meridional wind u_θ (figure not shown) and variation in geographic latitude (see Figures 9c and 9d). We have checked longitudinal variations of the meridional wind and found that the local time variation of the contribution of Coriolis force is mainly determined by the spatial distribution of the meridional wind, which reverses between day and night.

The peak longitudinal differences of ΔUy from these various runs were compared to the base run (all values were listed in Table 2). The differences between the base run and other runs were shown in Figure 11 (bottom). Red was for the daytime and black for the nighttime. The Northern Hemisphere was marked by circles and the Southern Hemisphere by asterisk. Positive values indicated that the longitudinal differences got enhanced when one of the factors in the model was changed. As expected, the ion drag tended to reduce the observed longitudinal differences of the zonal wind, because the peak longitudinal differences got larger when the ion drag was turned off. The effects were stronger at nighttime than at daytime. There was one exception at nighttime in the Northern Hemisphere, where the observed peak longitudinal difference was produced mainly by the ion drag.

The viscous effect was also negative on the observed longitudinal difference of the zonal wind, except at nighttime in the Southern Hemisphere. The effects were stronger at daytime than at nighttime. The Coriolis effects were negative in all cases on the observed ΔUy, with the daytime effects being quite comparable to the nighttime. The positive pressure gradient effects were much larger at nighttime than at daytime, and in the Southern Hemisphere they were more prominent than in the Northern Hemisphere.

4.6. Tidal Decomposition

Using CHAMP and Gravity Recovery and Climate Experiment observations, *Xiong et al.* [2015b] focused on the nonmigrating tidal signatures of the thermospheric mass density from 2007 to 2009 and of zonal wind from 2001 to 2003 that were associated with the MSNA features. They found that the zonal wind within 40°–60° MLat is dominated by the nonmigrating tidal components D0 and DW2 in both hemispheres, and their phases exhibited an antiphase relationship between the two hemispheres. For comparison, we decomposed the observed and modeled zonal wind within our latitudinal band 50°–60° MLat into nonmigrating tidal components. The amplitudes and phases of the largest components D0 and DW2 are shown in Table 3. The tidal phases in the model and observation were satisfactorily consistent, while the tidal amplitudes were not the same. However, the amplitude ratios between D0 and DW2 were comparable between the model and observation: DW2 was larger than D0 in the Northern Hemisphere and smaller in the Southern Hemisphere. A comparison with *Xiong et al.* [2015b] shows that we obtained generally larger amplitudes. This was probably due to the higher latitude of our study region. D0 and DW2 varied in antiphase in the two hemispheres, which was consistent with *Xiong et al.* [2015b] result. As discussed above, these harmonic components (D0 and DW2) and the interhemispheric antiphase relationship in the simulation are mostly caused by the pressure gradients induce by solar heating. The zonal wind plays an important role in the longitudinal distribution of the electron density through the transport process along the magnetic field lines, causing wave-2 and wave-1 patterns in the Northern and Southern Hemispheres, respectively [e.g., *Liu et al.*, 2010; *Zhang et al.*, 2011; *Xiong and Lühr*, 2014; *Wang et al.*, 2015].

5. Summary

In summary, we have presented the longitudinal difference patterns of the thermospheric zonal wind (ΔUy) in the subauroral region in different seasons and under solar flux conditions. We observed prominent wave-1 longitudinal and diurnal variation of ΔUy, which exhibited opposite variations in the two hemispheres. These structures persisted over the whole year and were independent of the solar activity. The nighttime longitudinal differences were larger than at daytime, and the southern differences were larger than the northern ones in local summer and winter. Model simulations confirmed the observed results of large-scale structures. The dipole tilt was found to be vital for the longitudinal variation of the zonal wind. The neutral air pressure gradient due to the difference in solar heating from day to night was a major contributor to the observed longitudinal differences in zonal wind. The pressure effects were larger at nighttime than at daytime and larger in the Southern Hemisphere than in the Northern Hemisphere. Our model runs confirmed that ion drag reduced the compatibility between modeled and observed ΔUy, with larger effects at nighttime than at daytime. However, the ion drag contributed to the observed peak longitudinal differences of ΔUy in the postmidnight sector in the Northern Hemisphere. The viscous force reduced the compatibility between modeled and observed longitudinal difference of the zonal wind, except at nighttime in the Southern Hemisphere. The Coriolis force also reduced the compatibility between modeled and observed longitudinal differences of the zonal wind but by a small amount. The sum of all these variables could explain reasonably well the observed local time and hemispheric asymmetry features of the longitudinal variations of the zonal wind at subauroral latitudes.

References

Aruliah, A. L., A. D. Farmer, D. Rees, and U. Brändström (1996), The seasonal behavior of high-latitude thermospheric winds and ion velocities observed over one solar cycle, *J. Geophys. Res.*, *101*, 15,701–15,712, doi:10.1029/96JA00360.

Bellchambers, W. H. (1958), Ionospheric measurements made at Halley Bay, *Nature*, *182*, 1596–1597, doi:10.1038/1821596a0.

Bilitza, D. (2001), International Reference Ionosphere 2000, *Radio Sci.*, *36*, 261–275, doi:10.1029/2000RS002432.

Blanc, M., and A. D. Richmond (1980), The ionospheric disturbance dynamo, *J. Geophys. Res.*, *85*, 1669–1686, doi:10.1029/JA085iA04p01669.

Buonsanto, M. J., and O. G. Witasse (1999), An updated climatology of thermospheric winds and F region ion drifts over Millstone Hill, *J. Geophys. Res.*, *104*, 24,675–24,687, doi:10.1029/1999JA900345.

Cnossen, I., and A. D. Richmond (2012), How changes in the tilt angle of the geomagnetic dipole affect the coupled magnetosphere-ionosphere-thermosphere system, *J. Geophys. Res.*, *117*, A10317, doi:10.1029/2012JA018056.

Codrescu, M. V., T. J. Fuller-Rowell, V. Munteanu, C. F. Minter, and G. H. Millward (2008), Validation of the Coupled Thermosphere Ionosphere Plasmasphere Electrodynamics model: CTIPE-Mass Spectrometer Incoherent Scatter temperature comparison, *Space Weather*, *6*, S09005, doi:10.1029/2007SW000364.

Deng, Y., Y. S. Huang, Q. Wu, J. Noto, D. Drob, and R. B. Kerr (2014), Comparison of the neutral wind seasonal variation from midlatitude conjugate observations, *J. Geophys. Res. Space Physics*, *119*, 3029–3035, doi:10.1002/2013JA019716.

Doornbos, E. V. D. I., H. Lühr, M. Förster, and G. Koppenwallner (2010), Neutral density and crosswind determination from arbitrarily oriented multiaxis accelerometers on satellites, *J. Spacecr. Rock.*, *47*, 580–589, doi:10.2514/1.48114.

Drob, D. P., et al. (2008), An empirical model of the Earth's horizontal wind fields: HWM07, *J. Geophys. Res.*, *113*, A12304, doi:10.1029/2008JA013668.

Emmert, J. T., B. G. Fejer, C. G. Fesen, G. G. Shepherd, and B. H. Solheim (2001), Climatology of middle- and low-latitude daytime F region disturbance neutral winds measured by Wind Imaging Interferometer (WINDII), *J. Geophys. Res.*, *106*, 24,701–24,712, doi:10.1029/2000JA000372.

Emmert, J. T., G. Hernandez, M. J. Jarvis, R. J. Niciejewski, D. P. Sipler, and S. Vennerstrom (2006), Climatologies of nighttime upper thermospheric winds measured by ground-based Fabry-Perot interferometers during geomagnetically quiet conditions: 2. High-latitude circulation and interplanetary magnetic field dependence, *J. Geophys. Res.*, *111*, A12303, doi:10.1029/2006JA011949.

Emmert, J. T., D. P. Drob, G. G. Shepherd, G. Hernandez, M. J. Jarvis, J. W. Meriwether, R. J. Niciejewski, D. P. Sipler, and C. A. Tepley (2008), DWM07 global empirical model of upper thermospheric storm-induced disturbance winds, *J. Geophys. Res.*, *113*, A11319, doi:10.1029/2008JA013541.

Erickson, P. J., F. Beroz, and M. Z. Miskin (2011), Statistical characterization of the American sector subauroral polarization stream using incoherent scatter radar, *J. Geophys. Res.*, *116*, A00J21, doi:10.1029/2010JA015738.

Fejer, B. G., J. Emmert, G. Shepherd, and B. Solheim (2000), Average daytime F region disturbance neutral winds measured by UARS: Initial results, *Geophys. Res. Lett.*, *27*(13), 1859–1862, doi:10.1029/2000GL003787.

Fejer, B. G., J. T. Emmert, and D. P. Sipler (2002), Climatology and storm time dependence of nighttime thermospheric neutral winds over Millstone Hill, *J. Geophys. Res.*, *107*, 1052, doi:10.1029/2001JA000300.

Fuller-Rowell, T. J., and D. S. Evans (1987), Height-integrated Pedersen and Hall conductivity patterns inferred from the TIROS-NOAA satellite data, *J. Geophys. Res.*, *92*, 7606–7618, doi:10.1029/JA092iA07p07606.

Hagan, M. E., M. D. Burrage, J. M. Forbes, J. Hackney, W. J. Randel, and X. Zhang (1999), GSWM-98: Results for migrating solar tides, *J. Geophys. Res.*, *104*, 6813–6828, doi:10.1029/1998JA900125.

Häusler, K., H. Lühr, S. Rentz, and W. Köhler (2007), A statistical analysis of longitudinal dependences of upper thermospheric zonal winds at dip equator latitudes derived from CHAMP, *J. Atmos. Sol. Terr. Phys.*, *69*, 1419–1430, doi:10.1016/j.jastp.2007.04.004.

Hedin, A. E. (1991), Extension of the MSIS thermosphere model into the middle and lower atmosphere, *J. Geophys. Res.*, *96*, 1159–1172, doi:10.1029/90JA02125.

Hedin, A. E., E. L. Fleming, A. H. Manson, F. J. Schmidlin, S. K. Avery, R. R. Clark, S. J. Franke, G. J. Fraser, T. Tsuda, F. Vial, and R. A. Vincent (1996), Empirical wind model for the upper, middle and lower atmosphere, *J. Atmos. Terr. Phys.*, *58*, 1421–1447.

Hernandez, G., and R. G. Roble (1984), The geomagnetic quiet nighttime thermospheric wind pattern over Fritz Peak Observatory during solar cycle minimum and maximum, *J. Geophys. Res.*, 89, 327–337, doi:10.1029/JA089iA01p00327.

Hernandez, G., D. P. Sipler, and M. A. Biondi (1978), Simultaneous measurements of midlatitude thermospheric winds at 105 deg W and 79 deg W longitude, *Geophys. Res. Lett.*, 5, 935–938, doi:10.1029/GL005i011p00935.

Kawamura, S., Y. Otsuka, S.-R. Zhang, S. Fukao, and W. L. Oliver (2000), A climatology of middle and upper atmosphere radar observations of thermospheric winds, *J. Geophys. Res.*, 105, 12,777–12,788, doi:10.1029/2000JA900013.

Killeen, T. L., and R. G. Roble (1988), Thermosphere dynamics: Contributions from the first 5 years of the Dynamics Explorer program, *Rev. Geophys.*, 26, 329–367, doi:10.1029/RG026i002p00329.

Killeen, T. L., J. W. Meriwether Jr., R. G. Roble, R. W. Smith, and N. W. Spencer (1986), Mean neutral circulation in the winter polar *F* region, *J. Geophys. Res.*, 91, 1633–1649, doi:10.1029/JA091iA02p01633.

Lin, C. H., J. Y. Liu, C. Z. Cheng, C. H. Chen, C. H. Liu, W. Wang, A. G. Burns, and J. Lei (2009), Three-dimensional ionospheric electron density structure of the Weddell Sea Anomaly, *J. Geophys. Res.*, 114, A02312, doi:10.1029/2008JA013455.

Liu, H., H. Lühr, S. Watanabe, W. KöHler, V. Henize, and P. Visser (2006), Zonal winds in the equatorial upper thermosphere: Decomposing the solar flux, geomagnetic activity, and seasonal dependencies, *J. Geophys. Res.*, 111, A07307, doi:10.1029/2005JA011415.

Liu, H., S. Watanabe, and T. Kondo (2009), Fast thermospheric wind jet at the Earth's dip equator, *Geophys. Res. Lett.*, 36, L08103, doi:10.1029/2009GL037377.

Liu, H., S. V. Thampi, and M. Yamamoto (2010), Phase reversal of the diurnal cycle in the midlatitude ionosphere, *J. Geophys. Res.*, 115, A01305, doi:10.1029/2009JA014689.

Lühr, H., K. Häusler, and C. Stolle (2007), Longitudinal variation of *F* region electron density and thermospheric zonal wind caused by atmospheric tides, *Geophys. Res. Lett.*, 34, L16102, doi:10.1029/2007GL030639.

Maus, S., et al. (2005), The 10th generation international geomagnetic reference field, *Phys. Earth Planet. Inter.*, 151, 320–322, doi:10.1016/j.pepi.2005.03.006.

Rees, D., T. Fuller-Rowell, and R. W. Smith (1980), Measurements of high latitude thermospheric winds by rocket and ground-based techniques and their interpretation using a three-dimensional time-dependent dynamical model, *Planet. Space Sci.*, 28, 919–932, doi:10.1016/0032-0633(80)90064-1.

Reigber, C., H. Lühr, and P. Schwintzer (2002), CHAMP mission status, *Adv. Space Res.*, 30, 129–134.

Richmond, A. D. (1992), Assimilative mapping of ionospheric electrodynamics, *Adv. Space Res.*, 12, 59–68, doi:10.1016/0273-1177(92)90040-5.

Richmond, A. D., C. Lathuillere, and S. Vennerstroem (2003), Wind in the high-latitude lower thermosphere: Dependence on the interplanetary magnetic field, *J. Geophys. Res.*, 108, 1066, doi:10.1029/2002JA009493.

Ridley, A. J., Y. Deng, and G. Tóth (2006), The global ionosphere-thermosphere model, *J. Atmos. Terr. Phys.*, 68, 839–864, doi:10.1016/j.jastp.2006.01.008.

Rishbeth, H. (1967), The effect of winds on the ionospheric F_2-peak, *J. Atmos. Terr. Phys.*, 29, 225–238, doi:10.1016/0021-9169(67)90192-4.

Rishbeth, H. (1972), Thermospheric winds and the *F* region: A review, *J. Atmos. Terr. Phys.*, 34, 1–47, doi:10.1016/0021-9169(72)90003-7.

Ritter, P., H. Lühr, and E. Doornbos (2010), Substorm-related thermospheric density and wind disturbances derived from CHAMP observations, *Ann. Geophys.*, 28, 1207–1220.

Sipler, D. P., B. B. Luokkala, and M. A. Biondi (1982), Fabry-Perot determinations of midlatitude *F*-region neutral winds and temperatures from 1975 to 1979, *Planet. Space Sci.*, 30, 1025–1032, doi:10.1016/0032-0633(82)90152-0.

Sipler, D. P., M. E. Hagan, M. E. Zipf, and M. A. Biondi (1991), Combined optical and radar wind measurements in the *F* region over Millstone Hill, *J. Geophys. Res.*, 96, 21,255–21,262, doi:10.1029/91JA02371.

Sun, Y.-Y., T. Matsuo, N. Maruyama, and J.-Y. Liu (2015), Field-aligned neutral wind bias correction scheme for global ionospheric modeling at midlatitudes by assimilating FORMOSAT-3/COSMIC h_mF_2 data under geomagnetically quiet conditions, *J. Geophys. Res. Space Physics*, 120, 3130–3149, doi:10.1002/2014JA020768.

Thayer, J. P., T. L. Killeen, F. G. McCormac, C. R. Tschan, J. Ponthieu, and N. W. Spencer (1987), Thermospheric neutral wind signatures dependent on the east-west component of the interplanetary magnetic field for Northern and Southern Hemispheres as measured from Dynamics Explorer-2, *Ann. Geophys.*, 5, 363–368.

Titheridge, J. E. (1995), Winds in the ionosphere: A review, *J. Atmos. Terr. Phys.*, 57(14), 1681–1714, doi:10.1016/0021-9169(95)00091-F.

Wang, H., H. Lühr, and S. Y. Ma (2005), Solar zenith angle and merging electric field control of field-aligned currents: A statistical study of the southern hemisphere, *J. Geophys. Res.*, 110, A03306, doi:10.1029/2004JA010530.

Wang, H., H. Lühr, K. Häusler, and P. Ritter (2011), Effect of subauroral polarization streams on the thermosphere: A statistical study, *J. Geophys. Res.*, 116, A03312, doi:10.1029/2010JA016236.

Wang, H., A. Ridley, and J. Zhu (2015), Theoretical study of zonal differences of electron density at midlatitudes with GITM simulation, *J. Geophys. Res. Space Physics*, 120, 2951–2966, doi:10.1002/2014JA020790.

Weimer, D. R. (2005), Improved ionospheric electrodynamic models and application to calculating Joule heating rates, *J. Geophys. Res.*, 110, A05306, doi:10.1029/2004JA010884.

Witasse, O., J. Lilensten, C. Lathuillere, and B. Pibaret (1998), Meridional thermospheric neutral wind at high latitude over a full solar cycle, *Ann. Geophys.*, 16, 1400–1409, doi:10.1007/s00585-998-1400-3.

Wu, Q., T. L. Killeen, and N. W. Spencer (1994), Dynamics Explorer 2 observations of equatorial thermospheric winds and temperatures: Local time and longitudinal dependences, *J. Geophys. Res.*, 99, 6277–6288, doi:10.1029/93JA02521.

Wu, Q., J. Noto, R. Kerr, S. Kapali, J. Riccobono, W. Wang, and E. R. Talaat (2014a), First Palmer and Millstone Hill midlatitude conjugate observation of thermospheric winds, *J. Geophys. Res. Space Physics*, 119, 3016–3028, doi:10.1002/2013JA019062.

Wu, Q., W. Yuan, J. Xu, C. Huang, X. Zhang, J.-s. Wang, and T. Li (2014b), First U.S.-China joint ground-based Fabry-Perot interferometer observations of longitudinal variations in the thermospheric winds, *J. Geophys. Res. Space Physics*, 119, 5755–5763, doi:10.1002/2014JA020089.

Xiong, C., and H. Lühr (2014), The Midlatitude Summer Night Anomaly as observed by CHAMP and GRACE: Interpreted as tidal features, *J. Geophys. Res. Space Physics*, 119, 4905–4915, doi:10.1002/2014JA019959.

Xiong, C., H. Lühr, and B. G. Fejer (2015a), Global features of the disturbance winds during storm time deduced from CHAMP observations, *J. Geophys. Res. Space Physics*, 120, 5137–5150, doi:10.1002/2015JA021302.

Xiong, C., Y.-L. Zhou, H. Lühr, and S.-Y. Ma (2015b), Tidal signatures of the thermospheric mass density and zonal wind at midlatitude: CHAMP and GRACE observations, *Ann. Geophys.*, 33, 185–196, doi:10.5194/angeo-33-185-2015.

Zhang, S.-R., J. C. Foster, A. J. Coster, and P. J. Erickson (2011), East-West Coast differences in total electron content over the continental US, *Geophys. Res. Lett.*, 38, L19101, doi:10.1029/2011GL049116.